Whole-Brain High-Resolution Metabolite Mapping with 3D Compressed-Sensing-SENSE-LowRank ^{1}H FID-MRSI

Antoine Klauser[1,2], Paul Klauser[3,4], Frédéric Grouiller[5,6], Sebastien Courvoisier[1,2], Francois Lazeyras[1,2]
[1] *Department of Radiology and Medical Informatics, University of Geneva, Switzerland*
[2] *Center for Biomedical Imaging (CIBM), Geneva, Switzerland*
[3] *Center for Psychiatric Neuroscience, Department of Psychiatry, Lausanne, Switzerland*
[4] *Service for Child and Adolescent Psychiatry, Department of Psychiatry, Lausanne, Switzerland*
[5] *Swiss Center for Affective Sciences, University of Geneva, Switzerland and*
[6] *Laboratory of Behavioral Neurology and Imaging of Cognition, Department of Fundamental Neuroscience, University of Geneva, Switzerland*
(Dated: May 18, 2020)

There is a growing interest of the neuroscience community to map the distribution of brain metabolites in vivo. Magnetic resonance spectroscopy imaging (MRSI) is often limited by either a poor spatial resolution and/or a long acquisition time which severely limits its applications for clinical or research purposes. We developed a novel acquisition-reconstruction technique combining fast ^{1}H-FID-MRSI sequence accelerated by random k-space undersampling and a low-rank and total-generalized variation (TGV) constrained model. This framework was applied to the brain of four healthy volunteers. Following 20 min acquisition, reconstruction and quantification, the resulting metabolic maps with a 5 mm isotropic resolution reflected the detailed neurochemical composition of all brain regions and revealed part of the underlying brain anatomy. Contrasts and features from the 3D metabolite distributions were in agreement with the literature and consistent across the four subjects. The successful combination of the 3D ^{1}H-FID-MRSI with a constrained reconstruction enables the detailed mapping of metabolite concentrations at high-resolution in the whole brain and with an acquisition time that is compatible with clinical or research settings.

I. INTRODUCTION

Measurement of the metabolite distributions in three dimensions (3D) over the whole human brain using proton magnetic resonance spectroscopic imaging (^{1}H-MRSI)has been the subject of 2 decades of intense research. From early multi-slices methods [1, 2] covering large portion of the brain to the first development of spatio-spectral encoding techniques [3–5] proposed by Mansfield [6], whole brain ^{1}H-MRSI unravels metabolic distributions with unique patterns and provides original physiological information complementary to usual MR imaging. Since then, 3D ^{1}H-MRSI human brain methods have been improved by implementation of acceleration techniques [7–9] or significant increase in spatial resolution [10, 11]. A complete and exhaustive overview of ^{1}H-MRSI techniques comprising also 2D approaches can be found in review articles [12–14].

Recently, advances in methods of reconstruction provided new solutions to the inherent limitations of ^{1}H-MRSI. The ^{1}H-MRSI acquisition geometry is often bounded to a rectangular volume-of-interest (VOI) with saturation of the outer signal to prevent skull lipid contamination, but latest work on efficient post-acquisition lipid decontamination [15–18] enables measurement of whole brain slices without limited VOI. Also, employing models including constraints of prior information for ^{1}H-MRSI data reconstruction significantly improves spectral quality and the resulting metabolite distributions [19, 20]. A priori knowledge of the underlying signal can also be exploited for super-resolution [21, 22] or drastic acceleration of ^{1}H-MRSI acquisition [23, 24].

The acquisition of whole-brain MRSI using traditional methods could be particularly lengthy due to the necessity to encode the large 4D(k-t) space. However, acquisition time can be significantly reduced by several techniques such as the free induction decay (FID)-MRSI acquisition, parallel imaging, and compressed sensing (CS). The FID-MRSI sequence known for its application in ^{31}P and other nuclei spectroscopic imaging [25, 26], has been more recently proposed for ^{1}H-MRSI [27, 28]. The simple sequence design dramatically shortens acquisition time in comparison with usual spin-echo methods by allowing low-flip-angle excitation and sub-second repetition time (TR). Implementation of parallel imaging techniques to 3D ^{1}H-MRSI of the human brain can reduce acquisition time by a factor of 2 to 8. [8, 9, 29]. Following the recent developments of CS for MRI [30, 31], the sparsity present in the 3D MRSI signal can also be exploited to accelerate the acquisition of the 4D encoding k-t space. The effectiveness of this approach was demonstrated for ^{13}C or ^{19}F [32, 33] as well as in combination with fast spatial-spectral encoding [34]. The application of CS to ^{1}H-MRSI of the human brain grants accelerations up to a factor of 4 but has been limited to 2D acquisitions[17, 35–38].

In this work we present original results of high-resolution 3D ^{1}H-MRSI of the whole human brain on a 3T clinical system. The acquisition-reconstruction schemes combine a fast FID-MRSI high-resolution sequence accelerated by random undersampling and reconstructed with a CS SENSE low-rank model (CS-SENSE-LR [17]) that has been extended to 3D in the present study. This comprehensive approach, combining FID and parallel acquisi-

tion schemes to CS-SENSE-LR reconstruction drastically shortens acquisition time and allows implementation of high-resolution 3D MRSI into clinical and research scanning protocols. Results of high resolution FID-MRSI acquisition combined with the CS-SENSE-LR reconstruction were previously presented in 2D at 3T field strength [17] and at 7T for 2D and 3D [39].

High-resolution metabolite mapping will find a great range of applications from neurology to psychiatry [40, 41]. In clinical neuroscience and with usual spectroscopic techniques, interpretation of spectroscopy findings is limited by the VOI approach, neglecting large cerebral parts around the volume selected by the a priori hypothesis. There is a strong need for whole-brain spectroscopy imaging which allows not only the mapping of metabolites in all brain regions but also the integration of brain spectroscopic data with other imaging modalities including structural and diffusion MR [42].

II. METHODS

A. Sequence and Acquisition

A ^{1}H-FID-MRSI [27, 28] sequence with a 3 dimensional phase encoding and WET [43] water suppression was implemented (Fig. 1) on a 3T Prisma fit MRI (Siemens, Erlangen, Germany) using a receiver head coil with $N_c = 64$ elements. A Shinnar-LeRoux optimized slab-selective excitation pulse of 0.9 ms was used optimized with a 9.5-kHz bandwidth. The acquisition delay between the excitation and the signal acquisition was shortened to echo time (TE) of 0.65 ms. A 4-kHz sampling rate FID was acquired with $T = 1024$ points and was followed by spoiler gradients and the repetition time (TR) was set to 355 ms. To avoid signal saturation considering the maximum T_1 value among metabolite to be 1400 ms [44], the excitation flip angle was set to 35 degrees. To avoid aliasing from signal outside the slab, two 30-mm-thick outer-volume saturation bands (OVS) were positioned right below and above the slab. The excited slab size was (A/P-R/L-H/F) 210 mm by 160 mm by 95 mm. The 3D encoding volume was set slightly larger to 210 mm by 160 mm by 105 mm to prevent again aliasing and with an encoding matrix of $42 \times 32 \times 20$ resulting in a $131\mu l$ voxel volume (5 mm isotropic). A fast reference water measurement was performed to determine the coil sensitivity profiles, with acquisition parameters identical to the main FID-MRSI sequence but without WET water suppression and with lower resolution $32 \times 24 \times 16$ (6.6 mm isotropic). The same encoding volume and slab were used but with 31-ms TR, 48 points in FID and a 5-degrees excitation flip angle. An anatomical 3D T_1-weighted MPRAGE sequence was also acquired during the session for navigation purpose and for anatomical segmentation of the volunteers' brain.

Sparse and random 3D phase-encoding MRSI raw data were acquired sparsely and randomly over the three-dimensional Fourier domain (k-space) to enable CS acceleration. The simple sequential spatial encoding method of the FID-MRSI sequence allows for a straightforward implementation of the random k-space sampling. During sequence preparation, a 3D mask was computed containing only k-space coordinates to be acquired. Defining $q = \sqrt{(k_x/k_x^{max})^2 + (k_y/k_y^{max})^2 + (k_z/k_z^{max})^2}$, the random sampling of the 3D mask was constrained to a density distribution following q^{-1} but with a fully-sampled spheroid of radius $q \leq \frac{1}{5}$ (Fig. 1). During the sequence acquisition, following the preparation, FID MRSI data are acquired following the k-space 3D mask.

B. MRSI data preprocessing and reconstruction model

Remaining water and lipid signal removal Residual water was removed using Hankel singular value decomposition (HSVD) method [45]. HSVD was applied separately to each coil element and time serie in the acquired points of the k-space. The lipid suppression was performed in k-space on the signal from each coil element using the metabolite-lipid spectral orthogonality technique [15, 17, 39]. The methods are described in details in previously published work [17].

CS-SENSE-LR reconstruction The CS approach requires to reconstruct sparsely-sampled MRSI data with an appropriate model that maximizes data fidelity while constraining spatial sparsity in metabolite distributions [30, 31]. We employed here a low-rank constrained model including total generalized variation (TGV) regularization [46]. We describe hereafter briefly the CS SENSE low-rank reconstruction (CS-SENSE-LR) that was previously described in [39]. MRSI raw data measured by phased array coil element $c = 1, \ldots, N_c$ at time t and at k-space coordinate $\mathbf{k}$ can be expressed with the forward model

$$s_c(\mathbf{k}, t) = \int_{\Omega \subset \mathbb{R}^3} \mathrm{e}^{2\pi \mathrm{i} \mathbf{k} \cdot \mathbf{r}} C_c(\mathbf{r}) B(\mathbf{r}, t) \rho(\mathbf{r}, t) d\mathbf{r}, \quad (1)$$

with 3D spatial coordinates $\mathbf{r}$ integrated over Ω the spatial support of the measured object and $\rho(\mathbf{r}, t) \in \mathbb{C}$ the transverse magnetization. $C_c(\mathbf{r}) \in \mathbb{C}$ represent the coil sensitivity profiles and $B(\mathbf{r}, t) = \mathrm{e}^{2\pi \mathrm{i} t \gamma \Delta B_0(\mathbf{r})}$ the spatial frequency shift caused by $\gamma \Delta B_0(\mathbf{r})$, the magnetic field inhomogeneity map (in Hz). The goal of the reconstruction is to retrieve the original $\rho(\mathbf{r}, t)$ from the sparsely sampled signal $s_c(\mathbf{k}, t)$ knowing $C_c(\mathbf{r})$ and $\Delta B_0(\mathbf{r})$.

The low-rank assumption implies a decomposition of the transverse magnetization in K spatial and temporal

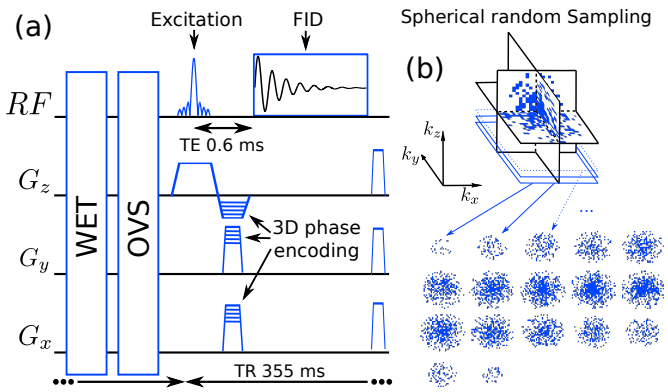

FIG. 1: Schematic of the FID-MRSI sequence with 3D phase encoding (left) preceded by the water suppression enhanced through T1 effects (WET) and outer-volume saturation bands (OVS) sequence blocs. An exemple of 3D undersampled k-space by factor 3.5 is shown (right)

components, $U_n(\mathbf{r}),\ V_n(t), n = 1, \ldots, K$:

$$\begin{aligned}\rho(\mathbf{r}, t) &= \sum_{n=1}^{K} U_n(\mathbf{r}) V_n(t) \\ &= \mathbf{U}(\mathbf{r})\mathbf{V}(t),\end{aligned} \tag{2}$$

with the last line employing vectorial notation. Considering discrete spatial and temporal sampling points, $s_c(\mathbf{k}, t), \mathbf{U}(\mathbf{r})\mathbf{V}(t)$ become multi-dimensional arrays $\mathbf{s}, \mathbf{U}, \mathbf{V}$ and the forward model (1) can read

$$\mathbf{s} = \mathcal{F}\mathcal{C}\mathcal{B}(\mathbf{UV}), \tag{3}$$

with the discrete Fourier transform operator $\mathcal{F}$ and $\mathcal{C}$ and $\mathcal{B}$ operators applying $C_c(\mathbf{r})$ and $B(\mathbf{r}, t)$ on discrete coordinates. After a first step consisting of remaining water removal and lipid signal suppression (described above) from $\mathbf{s}$, the discrete transverse magnetization $\rho = \mathbf{UV}$, is reconstructed $s_c(\mathbf{k}, t)$ with a 3D low-rank TGV model in [39, 47]. The TGV minimization problem [46] enable determination of the spatial and temporal components

$$\arg\min_{\mathbf{UV}} \ \|\mathbf{s} - \mathcal{F}\mathcal{C}\mathcal{B}(\mathbf{UV})\|_2^2 + \lambda \textstyle\sum_{n=1}^{K} \mathrm{TGV}^2\{U_c\} \tag{4}$$

. The coil sensitivity profiles, $C_c(\mathbf{r})$ were determined from the fast reference water acquisition using ESPIRiT [48] and $\Delta B_0(\mathbf{r})$ was estimated using *multiple signal classification algorithm* (MUSIC) [49] on the water signal from the same fast reference scan. By including coil sensitivity profiles and the TGV regularization that imposes sparsity in spatial first and second-order gradients, the CS-SENSE-LR reconstruction permits a faithful reconstruction of randomly sampled MRSI data [50, 51].

LCModel Quantification As final step, the reconstructed MRSI signal was fitted with LCModel [52] to quantifiy metabolite in each voxel separately. The LCModel basis was simulated using GAMMA package [53] and with parameters matching the acquisition sequence. The metabolite included in the basis were: N-acetylaspartate, N-acetyl aspartylglutamate, creatine, phosphocreatine, glycerophosphocholine, phosphocholine, myo-inositol, scyllo-inositol, glutamate, glutamine, lactate, gamma-aminobutyric acid, glutathione, taurine, aspartate, alanine. Lipid suppression by orthogonality as perform in this study might distort the baseline at 2ppm by the NAA singlet peak. To optimize LCModel fitting in presence of this distortion a singlet broad and inverted peak was added to the basis. It was simulated at 2 ppm with 20 Hz width and a $e^{i\pi}$ phase (opposite to NAA singlet). LCModel quantification estimates signal to noise (SNR) for each voxel [54] as spectral quality parameters. The Cramer-Rao Lower bound (CRLB) usually used as quantification error estimate for each metabolite is not valid anymore with the non-linear CS-SENSE-LR reconstruction.

C. Experiments

CS acceleration demonstration To demonstrate the CS acceleration capability and to assess of the metabolite maps reconstruction accuracy, a single MRSI acquisition without k-space undersampling was performed on a volunteer following the sequence details in II A but with a full elliptical k-space encoding instead and resulting in a 70 min acquisition. The raw data were first undersampled retrospectively to several extend to reproduce acceleration factors of $2, 3, 4, 5$ or 6 and following the same variable density undersampling that during the accelerated acquisition (described in II A). After undersampling of the raw data, metabolite maps were reconstructed following all the steps from II B. The TGV regularization parameter λ in 4 was adjusted on the fully-sampled dataset (3×10^{-4}) and was kept the same for all acceleration factors. The reconstructed spectral quality was assess at different acceleration and the fitting residual of the LCModel were quantified as quality parameter. The resulting metabolite maps were compared qualitatively and quantitatively with a normalized root

mean squared error (RMSE) and structural similarity index (SSIM).

Healthy volunteers accelerated acquisiton The accelerated FID-MRSI with accelerated acquisition was performed and reconstructed with the CS-SENSE-LR model on three volunteers to demonstrate reproducibility and robustness. Written informed consent was given by all the subjects before participation and the study protocol was approved by the institutional ethics committee. The FID-MRSI was acquired with acceleration factor 3.5 (20 min, optimal factor determined by the CS acceleration demonstration) for all three volunteers and were reconstructed with the same regularization as retrospective acceleration case, i.e. $\lambda = 3 \times 10^{-4}$. The spectral quality was presented with selected reconstructed spectra from four locations: the cingulate grey matter (GM), the frontal white matter (WM), the caudate nucleus and the temporal GM with the corresponding LCModel fitting.

Brain-atlas regional analysis To illustrate the metabolite contrasts and their relation to the underlying anatomical structures, the 3D metabolite maps were co-registered to an anatomical brain atlas. For each participant, T_1-weighted anatomical scans were segmented into gray and white matter compartment by using the computational anatomy toolbox (CAT12; http://www.neuro.uni- jena.de/cat) as implemented in statistical parametric mapping (SPM12) software (https://www.fil.ion.ucl.ac.uk/spm/software/spm12/) running in Matlab R2018b (The MathWorks, Inc., Natick, Massachusetts, US). Native-space gray matter images were spatially normalized to the DARTEL template in MNI standard space created from 555 healthy control subjects from the IXI-database (http://www.brain-development.org). Masks for the cerebral lobes were generated using the Standard atlas [55] in WFU PickAtlas toolbox (https://www.nitrc.org/projects/wfu_pickatlas/) and spatially transformed in participants' native space by applying the inverse of the transformation matrix generated during the spatial normalization step. Subcortical gray mater structures were automatically segmented using Freesurfer version 6.0.0 [56]. The resulting anatomical atlases were registered and downsampled to match the MRSI resolution and orientation (fig.5). Enventually, the mean, upper an lower quartiles were computed in each anatomical mask for each metabolite and all three subjects. These values were normalized by the same metabolite mean concentration from the whole brain and resulted in relative unitless concentration points. This data aim to highlight the consistency of the metabolite contrasts across subjects.

III. RESULTS

The results of the in vivo MRSI data accelerated retrospectively to illustrate the CS performance are shown in fig.2 for the 5 major metabolites measurable in 3T FID-MRSI: N-acetylaspartate + N-acetyl aspartylglutamate (tNAA), creatine + phosphocreatine (tCre), Choline moities metabolites (Cho) (choline, acetylcholine, phosphocholine and glycerophosphocholine), myo-inositol (Ins), glutamate + glutamine (Glx). The cortical layer is visible on tCr and Glx maps and the Cho distribution shows the highest signal intensity in frontal WM and the lowest values in occipital lobe. These spatial features remain clearly present while data are progressively randomly undersampled in the k-space from 50% to 17% (acceleration factor from 2 to 6). Although all dataset were reconstructed with the same value for regularization parameter λ, metabolite images that are strongly accelerated with factor > 4 miss fine detailed contrasts due to the lack of high k-space frenquencies remaining in the data.

The RMSE and SSIM of each metabolite volume relative to the 'no acceleration' volume show monotonic behaviors close to a linear relation with the acceleration factor in agreement with previous publications [38, 51]. Among all metabolite Glx shows always the highest RMSE and lowest SSIM. This is probably due to the lower signal of glutamine and glutamate in comparison to other metabolite. tNAA shows also higher error and lower similarity in comparison to tCre or Cho. This is possibly relative to the lipid suppression that can affect baseline at 2 ppm and add variability in the tNAA quantification.

Spectra shown at two location in the bottom of fig.2 exhibit no noticable change with acceleration. Possible spectra distortion resulting of the acceleration would also reflect in an increase of fitting residuals. But the residuals root mean square (RMS) average over the brain remains practically constant.

The full tNAA, tCre, Cho, Ins and Glx maps resulting from the accelerated acquisition (i.e 3.5) are displayed for volunteer 1 fig.3. The metabolite maps match the distribution features and have similar quality as for the retrospective acceleration by a factor 3 or 4 fig.2. Volumes of Cho and Glx concentrations which display the sharpest contrasts, and 4 sample spectra are presented in fig.4 for each of the three volunteers. The concentrations variations observed in the metabolite maps translate into visual spectral variations. The frontal WM spectrum shows clear higher Cho peak respective to other three locations and Cingulate GM and Temporal GM spectra present markedly higher Glx signal than Frontal WM and Caudate. These visual landmarks are noticeable for all three volunteers.

The spectra shown in fig.4 and fig.2 exhibit high SNR thanks to the low-rank constraint and a narrow linewidth due to the small voxel size in addition to the B_0 fieldmap correction in the CS-SENSE-LR model. Mean whole-

brain SNR estimated by LCModel was 14.2,12.7 and 12.6 for volunteers 1, 2 and 3. The mean spectral full width at half maximum was 5.67 Hz, 5.46 Hz and 5.19 Hz for the same subjects. The baseline distortion due to the lipid suppression by orthogonality is visible as a pit at 2 ppm forming a 'W' shape with the NAA peak. Nevertheless, the distortion is well fitted by the inverted broad peak added to the basis and the resulting baseline is smooth. This point is further addressed in the discussion.

The anatomical segmentation of 3D metabolite maps for volunteer 1 is illustrated in fig.5. Concentration plots for each region are shown in fig.6 and illustrates the robustness of anatomical contrasts: for all volunteers, the distribution of metabolite concentrations follow the same patterns. For tNAA, cortical concentrations tend to be lower in temporal lobes while subcortical concentrations are relatively high in the thalamus. Similarly, tCre concentrations are lower in temporal lobes than in other cortical regions. For Cho, plots show a lower concentration in GM than in WM as well as a high concentration in brain stem, hippocampus and amygdala. Distribution of Ins concentrations is particularly homogeneous when compared to the distribution of other metabolites. In contrast to Cho, Glx exhibits a consistent and markedly higher concentration in GM than in WM. For all metabolites, concentrations are relatively high in the cerebellum.

IV. DISCUSSION

There is a strong need for the whole-brain mapping of the metabolite distributions in fine details and within an acceptable time frame to allow its inclusion in scanning protocols running on regular 3T MR systems. For the first time, the unique combination of FID-MRSI with CS-SENSE-LR made possible the reconstruction of high-contrast and high-resolution 3D metabolite volumes following an acquisition limited to 20 min on a clinical 3T MRI.

The whole-brain approach coupled to the high-resolution (i.e. 5 mm isotropic) of the reconstructed volumes allowed a quantitative analysis of the brain metabolites across all brain regions. Among the 3 volunteers, we observed the same patterns of contrast between cerebral lobes, subcortical structures and GM/WM segments for each metabolite, suggesting the robustness of the measures.

The performance of the CS-SENSE-LR model in reconstructing undersampled dataset as depicted in fig.2 is demonstrated by the retrospective acceleration (or k-space sub-sampling) of a fully sampled 3D FID-MRSI. The random k-space spheroid sampling following a radius^{-1} distribution rule affects only the resulting spatial metabolite distributions without downgrading the spectral quality. This reconstruction property was highlighted by the qualitative and quantitative analysis of spectra after the retrospective acceleration in fig.2 and is also reported in previous work [38]. Strong acceleration results in loss of fine details or in a metabolite distribution smoothing due to the strong undersampling of the high k-space frequencies. Our results allowed us to determine an optimal acceleration factor, allowing both a dramatic acquisition-time reduction and a good metabolite mapping quality. Indeed, the optimal acceleration factor was found to be around 3.5.

The current application of the FID-MRSI CS-SENSE-LR method at high field (3T) compares as follow with ultra-high field (7T) [39]. The higher resonance frequency at 7T allows to acquire an FID with a given bandwith and number of points 7/3 faster than at 3T, and permits to shorten the TR and the acquisition time accordingly. On the other hand, 3T MRI show better B_0 shimming performances and more uniform B_1^+ profile in comparison to ultra-high setups, and allows FID-MRSI acquisition over larger FOVs covering the whole brain. We can note also that the SNR is twice lower at 3T in comparison with 7T acquisition and could represent a limitation for the spatial resolution. Though, in our protocol, the resolution was mostly limited by the acquisition duration and not the SNR as illustrated by the spectra in fig .4. The TGV regularization parameter used in the reconstruction was adjusted to $\lambda = 3 \times 10^{-4}$ on the fully-sampled dataset and is slightly lower than the previously found value in the 2D case ($\lambda = 10^{-3}$ in [17]). However, this same value was observed to be optimal for all 4 volunteer datasets. Therefore, the regularization parameter seems to depend mainly on the MRSI protocol and might require some minor adjustment when the slab thickness, the resolution, the flip-angle or other acquisition parameters are modified.

The acceleration factor 3.5 of our protocol provides a drastically shorter acquisition (20 min) in comparison to the fully sampled protocol (70 min). However, the MRSI acquisition, even accelerated, remains markedly long and is therefore susceptible to subject motion. While no motion correction or compensation were used in this study, the implementation of an interleaved imaging-based volumetric navigators could be expected to improve further the measurement accuracy and prevent possible motion artefact as shown in [57].

Although the lipid suppression by orthogonality performed as pre-processing removes efficiently any lipid signal from the brain spectra, it creates a specific distortion of the baseline at 2 ppm particularly visible in the spectra of fig.2 and less marked in fig.4. The distortion may strongly affects LCModel fitting performance that compensate the strong pit by an unrealistic 1st order phase correction impacting the quantification stability. We solved the issue by introducing a broad inverted peak in the LCModel basis that allows the distortion pit to be fitted as a negative peak while preserving the spectral phase and baseline estimation. Nevertheless, quantification of NAA and NAAG might be affected by the distortion. Further investigation would be necessary to ascertain the fitting quantification of these metabolites.

The 3D metabolite distributions observed over the

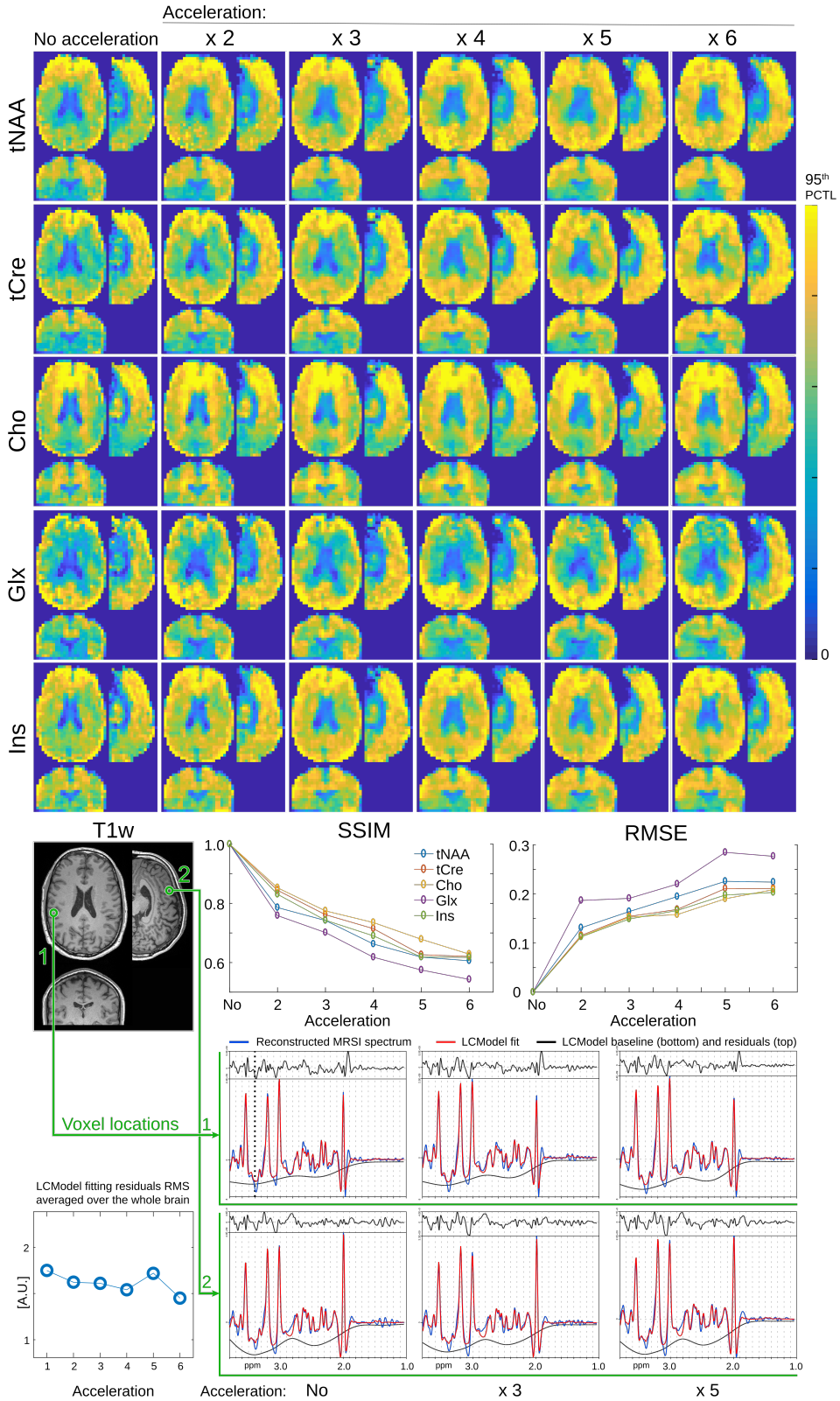

FIG. 2: Top, 3D FID-MRSI reconstructed metabolite volumes with retrospective acceleration. The fully sampled acquisition (No acceleration) was acquired in 70 min and acceleration factors correspond to k-space undersampling and reducing acquisition time accordingly (e.g. x3: 24 min, x6: 12 min). The color map was scaled individually for each metabolite range from 0 to the 95th percentile. Bottom, the normalized root mean squared error (RMSE) and structural similarity index (SSIM) computed for each metabolite map at all acceleration factors relative to the not accelerated result. Bottom, sample spectra from 2 distinct location are displayed and exhibit very little variation with the acceleration (no, 3, 5). The LCModel fit are shown with the fitting residuals. The root mean square (RMS) of the residuals averaged over the whole brain remains constant with the acceleration (bottom plot).

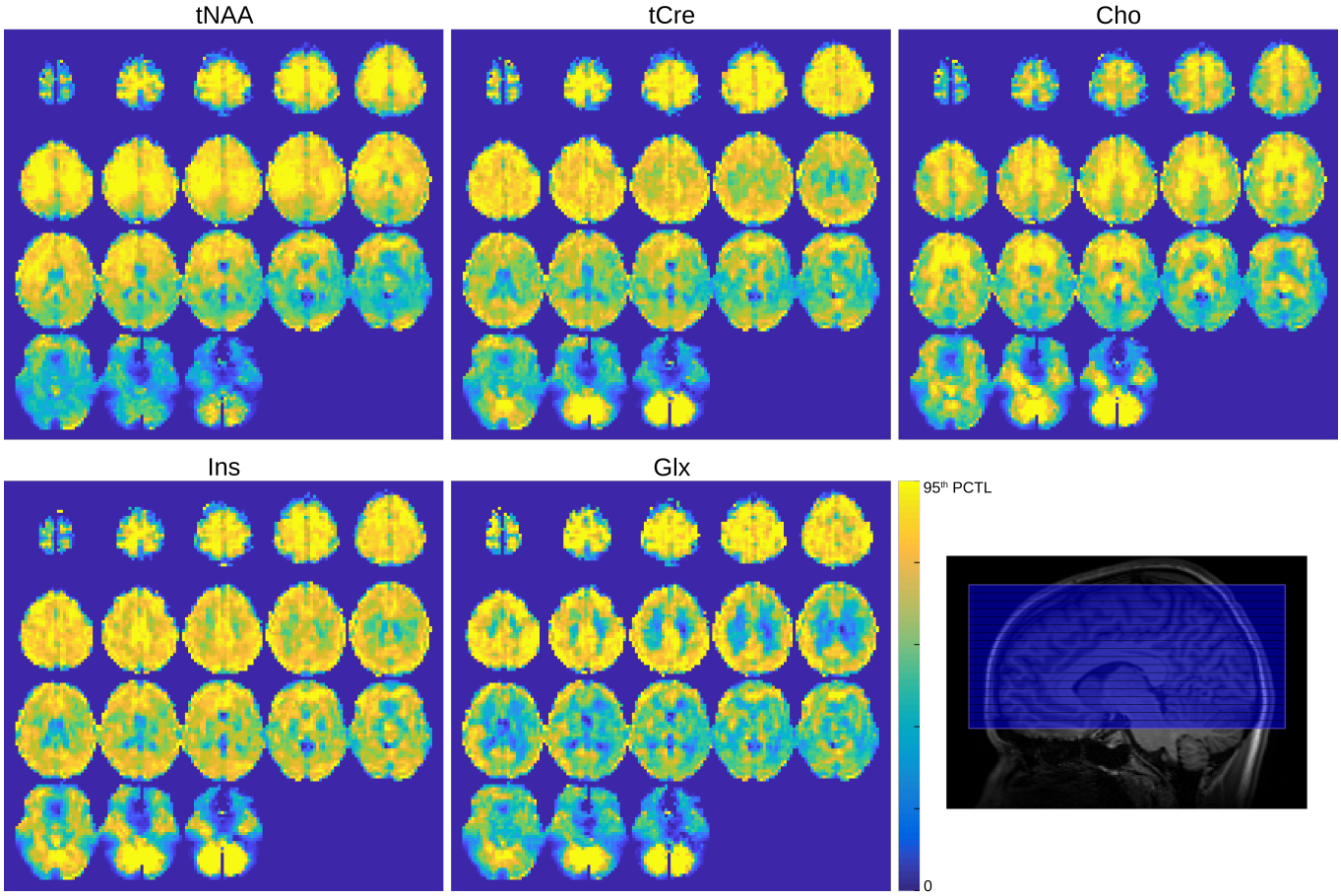

FIG. 3: CS-SENSE-LR 3D FID-MRSI measured on a healthy volunteer (volunteer 1) acquired in 20 min with acceleration factor 3.5 and resulting in tNAA, tCre, Cho, Ins and Glx maps. Color scale for each map span from 0 to the 95th percentile. Sagital T_1-weighted image (bottom right) show the location of the excitation slab (blue overlay).

whole brain in fig.2, 3 and 4 contained features and contrast described in III that are in agreement with previous publications. Thus, the distribution of tNAA, tCr, Cho are similar to the published data in [58, 59] and Glx in [10, 57, 60]. Thanks to the CS-SENSE-LR constrained reconstruction, the spectral quality is particularly good with a mean linewidth below 6 Hz for all three volunteers and a LCModel-estimated SNR above 12 for all of them. These encouraging results spark interest for applications of the CS-SENSE-LR reconstruction to other low-SNR MRSI acquisition strategies such as MEGA spectral-editing technique [14] or fast spatial-spectral encoding [13]. The steadiness of the segmentation results across subject in fig.6 illustrates qualitatively the sensitivity of the technique but an actual reproducibility study would be useful to assess the measurement variability and disentangle intersubject physiological difference from inter scan methodological variability.

To conclude, a novel acquisition-reconstruction scheme, coupling FID-MRSI with CS-SENSE-LR, makes possible 3D spectroscopic imaging of the whole human brain in high-resolution on a 3T system. The reconstructed metabolite volumes showed high anatomical contrast and high levels of features in 5 mm isotropic resolution. The resulting spectral quality demonstrated the efficiency of the model reconstruction for SNR enhancement and B_0 field map correction. Acceleration by random k-space undersampling allowed a dramatic reduction of the acquisition time from 70 to 20 min which makes its implementation in clinical or research protocols feasible. As proof of concept, metabolite volumes from three volunteers were segmented into anatomical lobes and substructures. The resulting contrast observed quantitatively is the counterpart of the metabolite features visible on 3D metabolite maps and are consistent through all three volunteers.

V. ACKNOWLEDGMENTS

PK supported by a fellowship from the Adrian and Simone Frutiger Foundation.

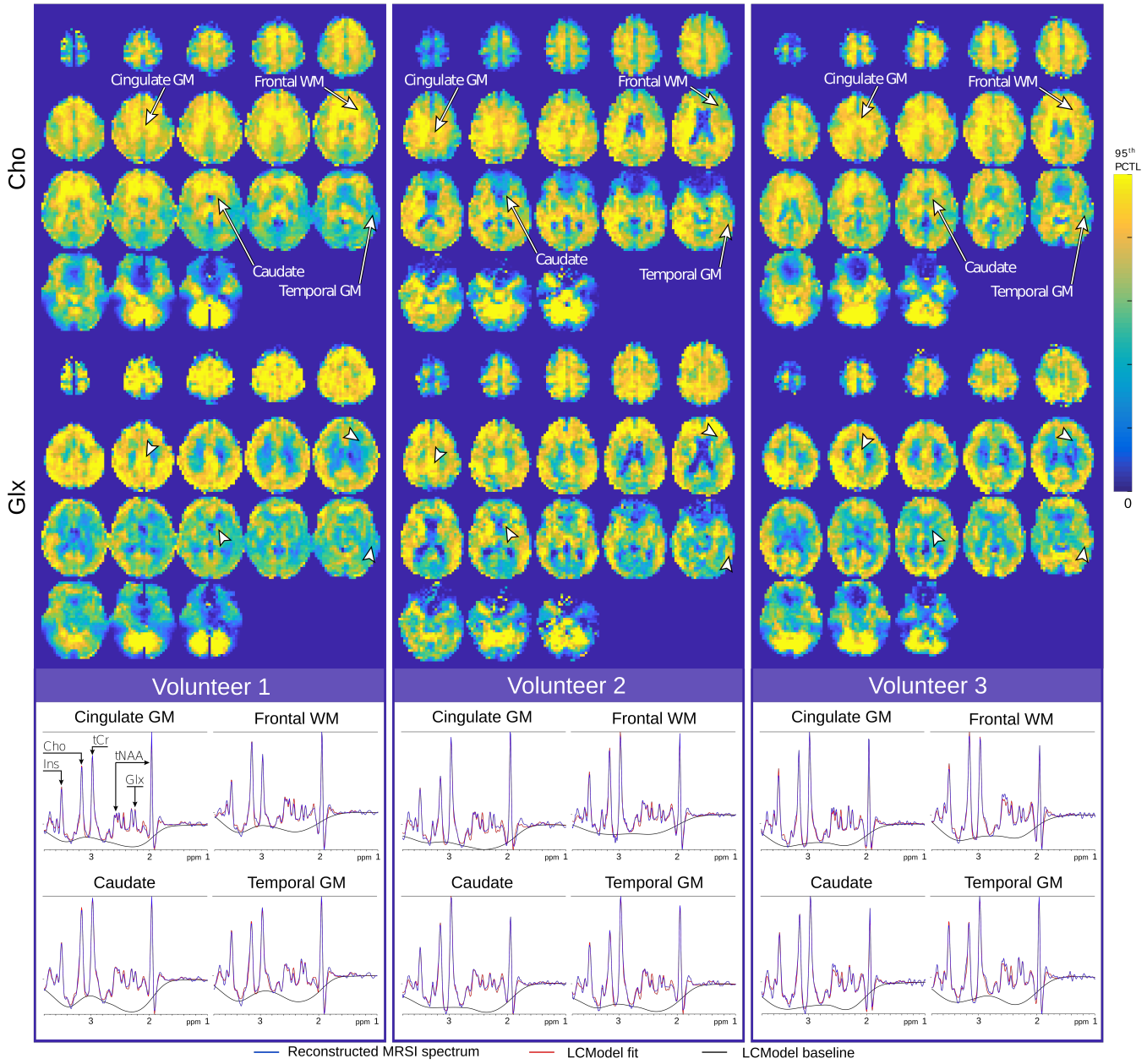

FIG. 4: Comparison of high-contrast Cho and Glx 3D maps measured with CS-SENSE-LR FID-MRSI on three healthy volunteers (volunteer 1,2 and 3) acquired in 20 min with acceleration factor 3.5. Color scale span from 0 to the 95th percentile of the respective metabolite concentration. Samples spectra originating from four distinct locations are shown for each volunteer. Cho and Glx signal amplitude in the spectra match the metabolite distribution observable on the maps.

[1] J. H. Duyn, J. Gillen, G. Sobering, P. C. van Zijl, and C. T. Moonen, Radiology **188**, 277 (1993), ISSN 0033-8419.

[2] G. Tedeschi, A. Bertolino, A. Righini, G. Campbell, R. Raman, J. H. Duyn, C. T. Moonen, J. R. Alger, and G. Di Chiro, Neurology **45**, 1384 (1995), ISSN 1526632X.

[3] S. Posse, C. DeCarli, and D. Le Bihan, Radiology **192**, 733 (1994), ISSN 0033-8419.

[4] E. Adalsteinsson, P. Irarrazabal, S. Topp, C. Meyer, A. Macovski, and D. M. Spielman, Magnetic Resonance in Medicine **39**, 889 (1998), ISSN 07403194.

[5] A. Ebel and A. A. Maudsley, Magnetic Resonance Imaging **21**, 113 (2003), ISSN 0730-725X.

[6] P. Mansfield, Magnetic Resonance in Medicine **1**, 370 (1984), ISSN 15222594.

[7] A. Ebel and N. Schuff, Magnetic Resonance in Medicine **58**, 1061 (2007), ISSN 07403194.

[8] R. Otazo, S.-Y. Tsai, F.-H. Lin, and S. Posse, Magnetic

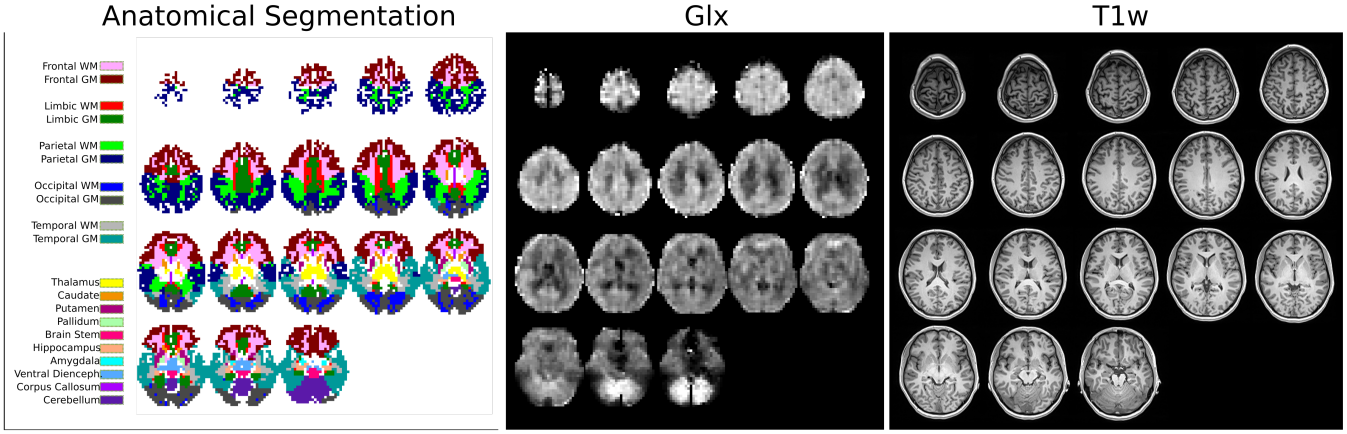

FIG. 5: The anatomical atlas for volunteer 1 resulting is shown (left). Glx concentration 3D map is shown for qualitative comparison in a grey scale (center) and the MPRAGE T_1-weighted images used to segment the volunteer anatomic parts.

Resonance in Medicine **58**, 1107 (2007), ISSN 07403194.

[9] X. Zhu, A. Ebel, J. X. Ji, and N. Schuff, Magnetic Resonance in Medicine **57**, 815 (2007), ISSN 07403194.

[10] P. Moser, W. Bogner, L. Hingerl, E. Heckova, G. Hangel, S. Motyka, S. Trattnig, and B. Strasser, Magnetic Resonance in Medicine **82**, 1587 (2019), ISSN 0740-3194.

[11] F. Lam, C. Ma, B. Clifford, C. L. Johnson, and Z.-P. Liang, Magnetic Resonance in Medicine **76**, 1059 (2016).

[12] P. B. Barker and D. D. Lin, Progress in Nuclear Magnetic Resonance Spectroscopy **49**, 99 (2006), ISSN 00796565.

[13] R. Vidya Shankar, J. C. Chang, H. H. Hu, and V. D. Kodibagkar, NMR in Biomedicine **32**, e4046 (2019), ISSN 09523480.

[14] K. Landheer, R. F. Schulte, M. S. Treacy, K. M. Swanberg, and C. Juchem, Journal of Magnetic Resonance Imaging p. jmri.26846 (2019), ISSN 1053-1807.

[15] B. Bilgic, B. Gagoski, T. Kok, and E. Adalsteinsson, Magnetic Resonance in Medicine **69**, 1501 (2013).

[16] C. Ma, F. Lam, C. L. Johnson, and Z. P. Liang, Magnetic Resonance in Medicine (2016), ISSN 15222594.

[17] A. Klauser, S. Courvoisier, J. Kasten, M. Kocher, M. Guerquin-Kern, D. Van De Ville, and F. Lazeyras, Magnetic Resonance in Medicine **81**, 2841 (2019), ISSN 07403194.

[18] S. Y. Tsai, Y. R. Lin, H. Y. Lin, and F. H. Lin, Magnetic Resonance in Medicine (2019), ISSN 15222594.

[19] R. Eslami and M. Jacob, IEEE Transactions on Medical Imaging **29**, 1297 (2010), ISSN 02780062.

[20] H. M. Nguyen, X. Peng, M. N. Do, and Z.-P. Liang, IEEE Trans Biomed Eng **60**, 78 (2013).

[21] R. Otazo, F.-H. Lin, G. Wiggins, R. Jordan, D. Sodickson, and S. Posse, Neuroimage **47**, 220 (2009).

[22] J. Kasten, A. Klauser, F. Lazeyras, and D. Van De Ville, J Magn Reson **263**, 193 (2016).

[23] F. Lam, C. Ma, B. Clifford, C. L. Johnson, and Z.-P. Liang, Magn Reson Med (2015).

[24] F. Lam, Y. Li, R. Guo, B. Clifford, and Z.-P. Liang, Magnetic Resonance in Medicine **83**, 377 (2020), ISSN 0740-3194.

[25] A. A. Maudsley, S. K. Hilal, W. H. Perman, and H. E. Simon, Journal of Magnetic Resonance (1969) **51**, 147 (1983), ISSN 00222364.

[26] R. Pohmann, M. von Kienlin, and A. Haase, Journal of Magnetic Resonance **129**, 145 (1997), ISSN 10907807.

[27] A. Henning, A. Fuchs, J. B. Murdoch, and P. Boesiger, NMR Biomed **22**, 683 (2009).

[28] W. Bogner, S. Gruber, S. Trattnig, and M. Chmelík, NMR in Biomedicine **25**, 873 (2012), ISSN 09523480.

[29] M. Sabati, J. Zhan, V. Govind, K. L. Arheart, and A. A. Maudsley, Journal of Magnetic Resonance Imaging **39**, 224 (2014), ISSN 10531807.

[30] D. Donoho, IEEE Transactions on Information Theory **52**, 1289 (2006), ISSN 0018-9448.

[31] L. Michael, D. David, and P. J. M., Magnetic Resonance in Medicine **58**, 1182 (2007).

[32] S. Hu, M. Lustig, A. Balakrishnan, P. E. Z. Larson, R. Bok, J. Kurhanewicz, S. J. Nelson, A. Goga, J. M. Pauly, and D. B. Vigneron, Magnetic Resonance in Medicine **63**, 312 (2010), ISSN 07403194.

[33] S. Hu, M. Lustig, A. P. Chen, J. Crane, A. Kerr, D. A. C. Kelley, R. Hurd, J. Kurhanewicz, S. J. Nelson, J. M. Pauly, et al., J Magn Reson **192**, 258 (2008).

[34] B. J. Geraghty, J. Y. C. Lau, A. P. Chen, and C. H. Cunningham, Magn Reson Med (2016).

[35] S. Geethanath, H.-M. Baek, S. K. Ganji, Y. Ding, E. A. Maher, R. D. Sims, C. Choi, M. A. Lewis, and V. D. Kodibagkar, Radiology **262**, 985 (2012), ISSN 0033-8419.

[36] I. Chatnuntawech, B. Gagoski, B. Bilgic, S. F. Cauley, K. Setsompop, and E. Adalsteinsson, Magnetic Resonance in Medicine **74**, 13 (2015), ISSN 07403194.

[37] N. E. Wilson, Z. Iqbal, B. L. Burns, M. Keller, and M. A. Thomas, Magnetic Resonance in Medicine **75**, 42 (2016), ISSN 07403194.

[38] S. Nassirpour, P. Chang, N. Avdievitch, and A. Henning, Magnetic Resonance in Medicine (2018), ISSN 15222594.

[39] A. Klauser, B. Strasser, B. Thapa, F. Lazeyras, and O. Andronesi, bioRxiv p. 2020.05.13.092668 (2020).

[40] G. Oz, J. R. Alger, P. B. Barker, R. Bartha, A. Bizzi, C. Boesch, P. J. Bolan, K. M. Brindle, C. Cudalbu, A. Dinçer, et al., Radiology (2014), ISSN 1527-1315.

[41] O. Ciccarelli, F. Barkhof, B. Bodini, N. D. Stefano, X. Golay, K. Nicolay, D. Pelletier, P. J. Pouwels, S. A. Smith, C. A. Wheeler-Kingshott, et al., The Lancet Neurology **13**, 807 (2014), ISSN 14744465.

[42] J. R. Bustillo, Dialogues in clinical neuroscience **15**, 329 (2013), ISSN 1958-5969.

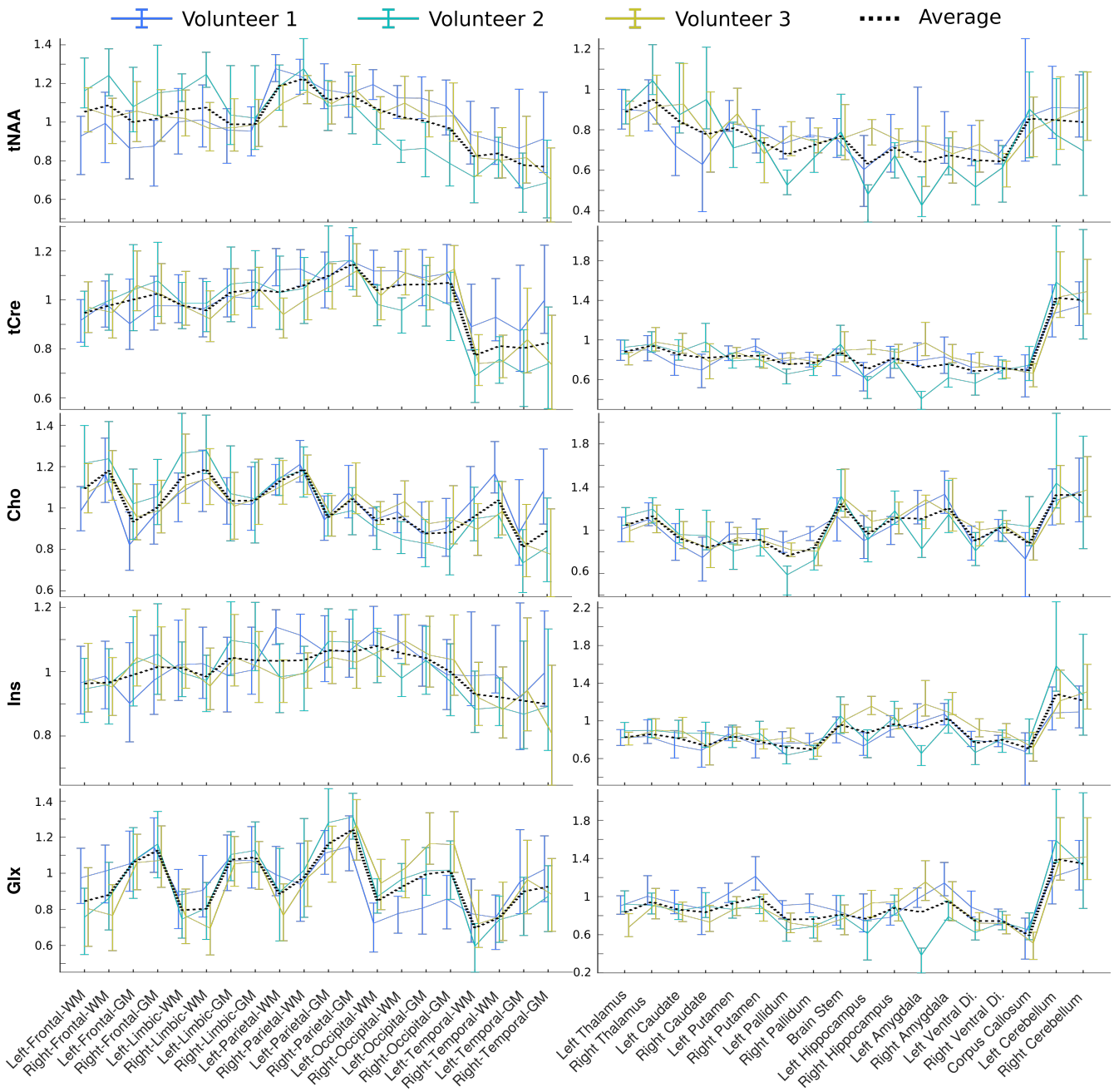

FIG. 6: Atlas metabolite content across three healthy volunteers based on anatomical segmentation (fig.5). Line-connected points correspond to the metabolite concentration mean in the respective anatomical area with the lower and upper quartiles as error bar for one subject. The dashed line represents the mean values accross the 3 subjects. Metabolite levels are normalized by the whole brain concentration value resulting in relative concentrations with a unit-less scale. Left plots represent relative concentrations in WM or GM in each lobe while right plots show relative concentrations in the deep GM.

[43] R. J. Ogg, P. B. Kingsley, and J. S. Taylor, Journal of Magnetic RSesonance. Series B **104**, 1 (1994), ISSN 10641866.

[44] F. Träber, W. Block, R. Lamerichs, J. Gieseke, and H. H. Schild, J Magn Reson Imaging **19**, 537 (2004), ISSN 10531807.

[45] H. Barkhuijsen, R. de Beer, and D. van Ormondt, Journal of Magnetic Resonance (1969) **73**, 553 (1987), ISSN 00222364.

[46] K. Bredies, K. Kunisch, and T. Pock, SIAM Journal on Imaging Sciences **3(3)**, 492 (2010), ISSN 19364954.

[47] J. Kasten, F. Lazeyras, and D. Van De Ville, Medical Imaging, IEEE Transactions on **32**, 1853 (2013).

[48] M. Uecker, P. Lai, M. J. Murphy, P. Virtue, M. Elad, J. M. Pauly, S. S. Vasanawala, and M. Lustig, Magnetic Resonance in Medicine **71**, 990 (2014), ISSN 07403194,

15334406.

[49] M. H. J. Gruber and M. H. Hayes, Technometrics **39**, 335 (1997), ISSN 00401706.

[50] D. Liang, B. Liu, J. Wang, and L. Ying, Magnetic resonance in medicine **62**, 1574 (2009), ISSN 1522-2594.

[51] R. Otazo, D. Kim, L. Axel, and D. K. Sodickson, Magnetic Resonance in Medicine **64**, 767 (2010), ISSN 07403194.

[52] S. W. Provencher, Magnetic Resonance in Medicine **30**, 672 (1993), ISSN 0740-3194.

[53] S. Smith, T. Levante, B. Meier, and R. Ernst, Journal of Magnetic Resonance, Series A **106**, 75 (1994), ISSN 10641858.

[54] S. W. Provencher, *LCModel Website*, URL `http://s-provencher.com/lcmodel.shtml`.

[55] J. A. Maldjian, P. J. Laurienti, R. A. Kraft, and J. H. Burdette, NeuroImage (2003), ISSN 10538119.

[56] B. Fischl, D. H. Salat, E. Busa, M. Albert, M. Dieterich, C. Haselgrove, A. van der Kouwe, R. Killiany, D. Kennedy, S. Klaveness, et al., Neuron **33**, 341 (2002), ISSN 08966273.

[57] P. Moser, K. Eckstein, L. Hingerl, M. Weber, S. Motyka, B. Strasser, A. Kouwe, S. Robinson, S. Trattnig, and W. Bogner, Magnetic Resonance in Medicine p. mrm.28076 (2019), ISSN 0740-3194.

[58] A. Maudsley, C. Domenig, V. Govind, A. Darkazanli, C. Studholme, K. Arheart, and C. Bloomer, Magnetic Resonance in Medicine **61**, 548 (2009), ISSN 07403194.

[59] T. V. Veenith, M. Mada, E. Carter, J. Grossac, V. Newcombe, J. Outtrim, V. Lupson, S. Nallapareddy, G. B. Williams, S. Sheriff, et al., PLoS One **9**, e115304 (2014).

[60] M. Z. Goryawala, S. Sheriff, and A. A. Maudsley, NMR in Biomedicine **29**, 1108 (2016), ISSN 10991492.